Numerical Local Upscaling For Elastic Rock Mechanical Properties

Mehdi Khajeh, Jeff Boisvert and Rick Chalaturnyk

Upscaling elastic geomechanical properties is important for reducing the computational requirements of geomechanical simulation while honoring local heterogeneities in rock properties. During simulation, elastic properties are often considered homogeneous; however, there is increasing interest in understanding the effect of heterogeneity on geomechanical simulation. Upscaling allows for the generation of realistically sized numerical models that can be simulated in a reasonable timeframe and also account for small scale heterogeneities. A novel local numerical upscaling technique is proposed to describe the macroscopic elastic behavior of complex heterogeneous media. This technique is compared to conventional analytical techniques and is shown to produce superior results when assessing the upscaling error of a synthetic facies model. The geomechanical response, (volumetric strain) of the coarse upscaled models is compared to the geomechanical response of the fine scale models. The proposed numerical technique producing results most similar to the fine scale model.

Introduction

The main objective of geomechanical simulation is to predict the deformation behavior of geo-materials when loads are applied. Rock mechanical properties, both elastic and plastic, are critical input parameters. Mechanical Earth Models (MEMs) are comprehensive geological models which include in-situ stress magnitudes/directions and also heterogeneous maps of rock mechanical properties. However, layer cake geo-models with constant elastic and plastic properties dominate the geomechanical field. Rather, heterogeneous MEM's are proposed in order to account for known rock heterogeneity and better predict the geomechanical response of an area of interest.

In addition to better predicting geomechanical response, the consideration of geostatistical techniques for generating static rock properties allows for the quantification of uncertainty through processing multiple realizations. The limiting factor in considering multiple realizations and fine scale heterogeneous property models is the CPU requirement of the geomechanical simulator (e.g. FLAC). This is the main motivation for considering upscaling. It is desirable to move from a high resolution/fine scale MEM that fully captures known heterogeneities to a low resolution/coarse scale model that responds in the same way as the fine scale MEM but can be simulated in a reasonable timeframe. Note that this is analogous to the well-established technique of permeability upscaling when considering flow simulation. Complex facies and property distributions (Figure 1a) and anisotropic deformation (Figure 1b) have not been considered in previous geomechanical upscaling techniques. A novel numerical upscaling technique for geomechanical properties is proposed. The technique is similar to local upscaling of permeability, but is applied to elastic properties. The methodology is demonstrated on a synthetic 2D example based on sand/shale distributions typical of the McMurray oil sands deposit located in northern Alberta, Canada. To assess the accuracy of the proposed methodology, conventional averaging techniques based on power law averaging are also considered.

Upscaling Petrophysical Properties

Porosity and permeability/transmissibility are the main petrophysical properties which are upscaled when considering flow simulation. Mathematically, upscaling of porosity could be written as:

$$\emptyset^* = \frac{1}{V_b} \int_{V_b} \emptyset\,(y) dV \tag{1}$$

Arithmetic, harmonic and geometric averaging (Equations 2, 3 and 4 respectively) can be used in permeability upscaling depending on the spatial arrangement of permeability. While harmonic and arithmetic averaging of permeability are theoretically appropriate for different flow problems, there is no similar theoretical framework for geomechanical simulation. A naïve upscaling technique for elastic rock properties would be the application of a power law average (Equation 5) with a calibrated w. In this work, these averaging techniques provide a baseline for the assessment of the proposed technique.

$$A^*_{arithmetic} = (\sum_{i=1}^{n} A_i h_i)/\sum_{i=1}^{n} A_i \tag{2}$$

$$A^*_{harmonic} = \sum_{i=1}^{n} L_i \Big/ \sum_{i=1}^{n} \left(\frac{L}{A}\right)_i \tag{3}$$

$$A^*_{geometric} = exp\frac{1}{n}\sum_{i=1}^{n} logA_i \tag{4}$$

$$A_w = \left(\frac{1}{n}\sum_{i=1}^{n} A_i^w\right)^{\frac{1}{w}} \tag{5}$$

where A is the property to be upscaled.

In addition to power law averaging, renormalization (Kin and Mansfield, 1999), REV-renormalization (Norris et al 1991) and full tensor averaging techniques (Kasap and Lake 1990) could be considered. These approaches are more sophisticated than power law averaging and have been shown to perform well for some classes of flow problems. However, similar techniques are not generally available for geomechanical properties and comparison for this work is limited to the aforementioned averaging techniques.

There are four general strategies for upscaling, typically applied to upscaling permeability:

- Local upscaling
- Extended local upscaling
- Local-global (quasi global) upscaling
- Global upscaling

Local upscaling (Durlofsky 1991; Pickup et al 1994; and Durlofsky 2005) is the solution of the governing physical equations (i.e. fine scale pressure equation for flow) with an assumed boundary condition for the fine grid blocks that are contained in a single coarse cell (Figure 2a). The cells surrounding the coarse block of interest are ignored. Different boundary conditions are often considered with constant pressure and no flow boundaries (Figures 2b and 2c). Effective properties (i.e. permeability) in different directions are obtained. From the configurations shown in Figure 2b and 2c, effective properties in the horizontal and vertical directions (i.e. K^*_x and K^*_y) can calculated.

Upscaling Elastic properties

In addition to the techniques mentioned for analytically upscaling permeability/transmissibility, several analytical techniques have been developed for upscaling and homogenization of elastic media. Mackenzie (1950) used a self-consistent model to determine the equivalent elastic media (EEM) of a material composed of three phases. Hashin (1995), Backus (1962), Hill (1965), Budiansky (1965) and Salamon (1968) developed other analytical formulations for equivalent elastic media calculation. Although different assumptions are considered in these approaches, a common element is their consideration of a simplified stratified facies configuration which is not appropriate for the complex facies configurations typically found in the McMurray formation.

Numerical techniques for upscaling of elastic properties are not common. Elkateb (2003) proposed a mathematical expression for the determination of equivalent elastic moduli for a simplified layer cake model with isotropic elastic deformation. However, the deformation behavior of many materials depends upon orientation. That is, the stress-strain response of a sample taken from the material in one direction will be different if the sample were taken in different directions. In this case, the assumption of isotropic deformation may result in significant error. In the proposed upscaling technique, both complex heterogeneous material and anisotropic deformation are considered.

Proposed Methodology for Numerical Upscaling of Elastic Properties

Conceptually, the numerical upscaling of elastic geomechanical properties is shown in Figure 3. When considering heterogeneous media (Figure 3a) the loading process would result in complex deformation (Figure 3b). After upscaling this system to a single block, the goal is to reproduce the average fine scale deformation in the coarse scale block (Figure 3c). The coarse upscaled property (yellow color in Figure 3c) is the value that results in the average displacement had the fine scale model been deformed. The remainder of this section details each step of the upscaling process.

The general form of Hooke's Law, comprehensively used in the classical theory of elasticity is:

$$\sigma_{ij} = A_{ijmn}e_{mn} \tag{6}$$

where σ_{ij} is the 2nd order stress tensor, e_{mn} is the 2nd order strain tensor and A_{ijmn} is a general form of the 4th order elastic tensor. Depending on the material under study, a media could be considered homogeneous/heterogeneous and isotropic/anisotropic. In the case of heterogeneous material the characteristic tensor is described by Equation 7. Using more convenient notation, Hooke's Law is given by Equation 8.

$$A_{ijmn} = A_{ijmn}(x, y, z) \tag{7}$$

$$\begin{bmatrix} \sigma_x \\ \sigma_y \\ \sigma_z \\ \tau_{zy} \\ \tau_{zx} \\ \tau_{xy} \end{bmatrix} = \begin{bmatrix} A_{11} & A_{12} & A_{13} & A_{14} & A_{15} & A_{16} \\ A_{21} & A_{22} & A_{23} & A_{24} & A_{25} & A_{26} \\ A_{31} & A_{32} & A_{33} & A_{34} & A_{35} & A_{36} \\ A_{41} & A_{42} & A_{43} & A_{44} & A_{45} & A_{46} \\ A_{51} & A_{52} & A_{53} & A_{54} & A_{55} & A_{56} \\ A_{61} & A_{62} & A_{63} & A_{64} & A_{65} & A_{66} \end{bmatrix} \begin{bmatrix} e_x \\ e_y \\ e_z \\ e_{zy} \\ e_{zx} \\ e_{xy} \end{bmatrix} \tag{8}$$

Micro features commonly arise in natural and synthetic materials in such a way as to produce a stress-strain response with particular symmetries. The elastic characteristic matrix A_{ijmn} (or in contracted form, A_{ij}) can be simplified with reasonable symmetry assumptions. Orientations for which an anisotropic material has the same stress-strain response can be determined by coordinate transformation. Transversely isotropic deformation is commonly assumed and specifies that a material possess an axis of symmetry of order n when the elastic moduli remains unchanged for rotations of 2π/n radians about the axis (Figure 4). The elasticity stiffness matrix, assuming transverse isotropy, reduces to Equation 9.

$$\begin{bmatrix} A_{11} & A_{12} & A_{13} & 0 & 0 & 0 \\ A_{21} & A_{11} & A_{23} & 0 & 0 & 0 \\ A_{31} & A_{32} & A_{33} & 0 & 0 & 0 \\ 0 & 0 & 0 & A_{44} & 0 & 0 \\ 0 & 0 & 0 & 0 & A_{44} & 0 \\ 0 & 0 & 0 & 0 & 0 & (A_{11} - A_{12})/2 \end{bmatrix} \tag{9}$$

Thus, the elasticity matrix for the transversely isotropic case reduces to having only five independent stiffnesses. Further simplification of this system is obtained by assuming plane strain. If the dimension of the body in one direction, x_3, is considerably larger than the dimension of body in other two directions, it can be said that displacement in that direction would be zero. In other words:

$$U_1 = u_1(x_1, x_2)$$
$$U_2 = u1(x_1, x_2)$$
$$U_3 = \text{constant} \tag{10}$$

And as a result it can be assumed that

$$e_{33} = e_{32} = ee_{31} = 0 \tag{11}$$

If the dimension of the body in one direction, x3, is considerably smaller than the dimension of the body in the other two directions, σ33= σ 32= σ33= e32=e31= 0 but e33 is not zero. In the proposed methodology, the plane strain condition is considered to reduce the dimensionality of the problem. Thus, Hooke's Law in the case of transverse isotropy and plane strain simplifies to:

$$\begin{bmatrix} e_{11} \\ e_{22} \\ 0 \\ e_{12} \end{bmatrix} = \begin{bmatrix} a_{11} & a_{12} & a_{13} & 0 \\ a_{21} & a_{22} & a_{23} & 0 \\ a_{31} & a_{32} & a_{33} & 0 \\ 0 & 0 & 0 & 1/2G' \end{bmatrix} \begin{bmatrix} \sigma_{11} \\ \sigma_{22} \\ \sigma_{33} \\ \sigma_{12} \end{bmatrix} \tag{12}$$

In terms of elastic properties, young modulus (E) and poison's ratio (v):

$$\begin{bmatrix} e_{xx} \\ e_{yy} \\ 0 \\ e_{xy} \end{bmatrix} = \begin{bmatrix} 1/E_x & -v_{yx}/E_y & -v_{zx}/E_z & 0 \\ -v_{xy}/E_x & 1/E_y & -v_{zy}/E_z & 0 \\ -v_{xz}/E_z & -v_{yz}/E_y & 1/E_z & 1/2G' \\ 0 & 0 & 0 & \end{bmatrix} \begin{bmatrix} \sigma_{xx} \\ \sigma_{yy} \\ \sigma_{zz} \\ \sigma_{xy} \end{bmatrix} \tag{13}$$

where E_i is Young modulus in tension/compression and v_{ij} is poison's ratio characterizing contraction in the direction of one axis when tension is applied in a different direction. For example, v_{yx} is the ratio characterizing the contraction in x when tension is applied in y. Assuming X-Z is the plane of symmetry:

$$E_x = E_z$$
$$v_{xz} = v_{zx}$$
$$v_{xy} = v_{zy} \tag{14}$$

By considering:

$$E_x = E_z = xm$$
$$E_y = ym$$
$$v_{xz} = v_{zx} = nux$$
$$v_{xy} = v_{zy} = nuy$$

(15)

where;

xm: is young modulus in the plane of symmetry

ym: is young modulus in the plane perpendicular to the plane of symmetry

nux: Poisson's ratio for the normal strain in the x-direction (in the plane of isotropy) related to the normal strain in the z-direction due to uniaxial stress in the z-direction

nuy: Poisson's ratio for the normal strain in the y-direction (in the plane perpendicular to the plane of isotropy) related to the normal strain in the x-direction (in the Plane of isotropy) due to uniaxial stress in the x-direction. By knowing:

$$v_{xy}/E_x = v_{yx}/E_y$$

(16)

Equation 13 is simplified to:

$$
\begin{bmatrix} e_{xx} \\ e_{yy} \\ 0 \\ e_{xy} \end{bmatrix} = \begin{bmatrix} 1/xm & -nuy/xm & -nux/xm & 0 \\ -nuy/xm & 1/E_y & -nuy/xm & 0 \\ -nux/xm & -nuy/xm & 1/xm & 1/2G' \\ 0 & 0 & 0 & \end{bmatrix} \begin{bmatrix} \sigma_{xx} \\ \sigma_{yy} \\ \sigma_{zz} \\ \sigma_{xy} \end{bmatrix}
$$

(17)

Five parameters are required to fully characterize the problem under the above assumptions: xm, ym, nux, nuy and G' (G_{xy}) which is the shear modulus between the plane of isotropy and the perpendicular plane. With good approximation, G' (G_{xy}) can be determined from Equation 18 (Lekhnittskii 1981).

$$G_{xy} = \frac{E_x E_y}{E_x(1 + 2v_{xy}) + E_y}$$

(18)

The upscaling process reduces to determining the value of these five parameters for a coarse cell that results in the same average displacement as the fine scale model (Figure 3).

The general workflow is:

Step 1: Solve the transversely isotropic Hooke's law (Equation 17) for the boundary of the target coarse scale cell. In this step the elastic tensor, (LHS matrix in Equation 17), is calculated and the non-uniformly deformed body (Figure 3b) is obtained.

Step 2: Average the displacement on the border of the coarse scale body. In this step, the hatched black rectangle (Figure 3c) is obtained.

Step 3: Calculate the characteristic elastic parameters which results in the same stress and strain tensor applied on the uniformly deformed body. In this step, Equation 17 is solved again for the uniformly deformed body.

G' is determined from Equation 18, thus there are four unknowns determined from the uniform stress and strain tensors. The number of equations obtained in a single loading configuration is less than the number of unknowns; therefore, it is not possible to determine all required values by applying one stress configuration. Two different initial boundary conditions are considered. Figure 5 shows the initial boundary conditions for the first (top) and second (bottom) loading scenarios, where,

L_1 is the initial length of coarse scale cell in the X direction.

L_2 is the initial length of coarse scale cell in the Y direction.

i is the number of fine scale cells in the X direction of the coarse scale cell.

j is the number of fine scale cells in the Y direction of the coarse scale cell

Hooke's Law (Equations 19 and 20) are considered for the uniformly deformed body as a result of the first and second loading scenarios.

$$
\begin{bmatrix} <e^1_{11}> \\ <e^1_{22}> \\ 0 \end{bmatrix} = \begin{bmatrix} 1/xm & -nuy/xm & -nux/xm \\ -nuy/xm & 1/E_y & -nuy/xm \\ -nux/xm & -nuy/xm & 1/xm \end{bmatrix} \begin{bmatrix} <\sigma^1_{11}> \\ 0 \\ <\sigma^1_{33}> \end{bmatrix}
$$

(19)

$$\begin{bmatrix} <e^2_{11}> \\ <e^2_{22}> \\ 0 \end{bmatrix} = \begin{bmatrix} 1/xm & -nuy/xm & -nux/xm \\ -nuy/xm & 1/E_y & -nuy/xm \\ -nux/xm & -nuy/xm & 1/xm \end{bmatrix} \begin{bmatrix} 0 \\ <\sigma^2_{22}> \\ <\sigma^2_{33}> \end{bmatrix}$$

(20)

where,

$<\sigma^1_{33}>$ and $<\sigma^2_{33}>$ is the average σ_{33} as a result of the first and second loading configuration.

$<e^1_{11}>$, $<e^1_{22}>$ and $<e^2_{11}>$, $<e^2_{22}>$ are the equivalent strain components for the uniformly deformed body for the first and second loading scenarios. These can be obtained from:

$$\langle e_{11} \rangle = \frac{(\sum_{(i)} xdisp_l)/i + (\sum_{(i)} xdisp_r)/i}{L_1}$$

(21)

$$\langle e_{22} \rangle = \frac{(\sum_{(j)} ydisp_t)/j + (\sum_{(j)} ydisp_b)/j}{L_2}$$

where,

$(\sum_{(i)} xdisp_l)/i$: Average displacement of the fine scale cells on the left hand boundary of the coarse cell.

$(\sum_{(i)} xdisp_r)/i$: Average displacement of the fine scale cells on the right hand boundary of the coarse cell.

$(\sum_{(j)} ydisp_t)/j$: Average displacement of fine scale cells on the top boundary of the coarse cell.

$(\sum_{(j)} ydisp_b)/j$: Average displacement of fine scale cells on the bottom boundary of the coarse cell.

From these loading configurations, the following system of equations (Equation 22 for the first loading scenario and Equation 23 for the second) are obtained.

$$\langle e^1_{11} \rangle = \left(\frac{1}{xm}\right)\langle\sigma^1_{11}\rangle + \left(\frac{-nux}{xm}\right)\langle\sigma^1_{33}\rangle \qquad (a)$$

$$\langle e^1_{22} \rangle = \left(\frac{-nuy}{xm}\right)\langle\sigma^1_{11}\rangle + \left(\frac{-nuy}{xm}\right)\langle\sigma^1_{33}\rangle \qquad (b)$$

(22)

$$0 = \left(\frac{-nux}{xm}\right)\langle\sigma^1_{11}\rangle + \left(\frac{1}{xm}\right)\langle\sigma^1_{33}\rangle \qquad (c)$$

$$\langle e^2_{11} \rangle = \left(\frac{-nuy}{xm}\right)\langle\sigma^2_{22}\rangle + \left(\frac{-nux}{xm}\right)\langle\sigma^2_{33}\rangle \qquad (a)$$

$$\langle e^2_{22} \rangle = \left(\frac{1}{ym}\right)\langle\sigma^2_{22}\rangle + \left(\frac{-nuy}{xm}\right)\langle\sigma^2_{33}\rangle \qquad (b)$$

(23)

$$0 = \left(\frac{-nuy}{xm}\right)\langle\sigma^2_{22}\rangle + \left(\frac{1}{xm}\right)\langle\sigma^2_{33}\rangle \qquad (c)$$

From these systems of equations, elastic characteristic parameters of the upscaled cell can be calculated. This process is repeated for all coarse cells.

Synthetic Model

Consider a synthetic reservoir surrounded by side, under and overburden (Figure 6). This geometry is used to test the proposed methodology with the goal of predicting the response of the central reservoir. Using sequential indicator simulation (SIS) a heterogeneous facies model is generated for the central zone of interest. The side, under and overburdens are included to minimize boundary effects and are assumed homogeneous (Table 1). Table 2 summarizes the number of cells used in each zone for the fine scale model.

The heterogeneous central zone is modeled with unconditional SIS (Figure 7) using GSLIB (Deutsch and Journel 1998). A realistic shale proportion of 20% is assumed. Note that rock properties are assumed homogenous within each facies (Table 1). Sequential Gaussian simulation could be used to better characterize the expected within facies heterogeneity; however, for the purposes of demonstrating the proposed upscaling methodology, a homogenous model within each facies is adequate.

Error Analysis

The error resulting from upscaling is assessed by comparing the geomechanical response of the fine scale model (Figure 7) to the response of the coarse upscaled models using power law averaging and the proposed numerical

upscaling. Volumetric strain is considered as the geomechanical response of interest, but vertical displacement profiles, normal strains or shear strain distributions could be considered. The error used is given in Equation 24.

$$[\%]e = \frac{\sum_r \left|1 - \frac{\overline{e_{v_r}}}{e_{v_r}}\right|}{n_r} * 100 \tag{24}$$

where,

$\overline{e_{v_r}}$ is the average volumetric strain of the fine scale cells in the rth upscaled block, Equation 25.
e_{v_r} is the volumetric strain in the rth upscaled block.
n_r is the number of blocks in the upscaled model.

$$\overline{e_{v_r}} = \frac{\sum_i e_{v_i}}{n_i} * 100 \tag{24}$$

where,

e_{v_i} is the volumetric strain in the ith fine scale cell within the upscaled block.
n_i is the number of fine scale cells in each upscaled block.

Various upscaling ratios (number of fine scale cells in each upscaled block) are considered to assess the upscaling methodology. In total, 15 upscaling ratios are considered; horizontal ratios of 1:1, 5:1, 15:1, 30:1, 60:1, 100:1 and vertical ratios of 1:1, 4:1 and 8:1.

Results

One of the main purposes of upscaling is to reduce the geomechanical simulation runtime. Considering fewer cells in the model has a significant effect on the CPU time (Figure 8). For this study FLAC (ITASCA®) is used as geomechanical simulator.

In Figures 9 and 10 the results of upscaling of Young Modulus for selected horizontal upscaling ratios and just for arithmetic and proposed numerical (xm) upscaling techniques are shown for vertical upscaling ratios of 1:1 and 1:4 respectively. Similar results are obtained for other ratios. In Figure 11 the results of upscaling of Young Moduli in plane of isotropy (xm) and perpendicular to plane of isotropy (ym) for vertical upscaling ratio of 8:1 and for selected horizontal upscaling ratios are shown.

Averaging in the vertical direction has a larger effect on upscaling because of the shorter vertical variogram range typical of the McMurray formation. The effect of considering a 30:1 horizontal ratio is minimal as shale's are typically more continuous horizontally, but a 4:1 ratio vertically is significant. The visual difference in the upscaled results between averaging and the proposed numerical technique (Figures 9 and 10) appear minimal; however, the resulting volumetric strain error is significant. Using the error definition (Equation 24) the effect of different upscaling processes on volumetric strain is clear (Figures 12 and 13). The proposed numerical averaging technique is superior for all vertical and horizontal ratios considered. Note that it is possible that considering a different power (Equation 5) may result in lower error. Moreover, only a single SIS realization was considered, further testing on other configurations and incorporating within facies heterogeneities using SGS is required.

Discussion and Conclusion

A novel numerical local upscaling technique for elastic properties is proposed. Upscaling error was assessed by considering volumetric strain as the geomechanical response and indicated that the proposed numerical technique has promise. Further comparisons to existing analytical techniques and application to existing reservoirs is required to fully validate the methodology. In addition to volumetric strain, the vertical displacement profile should be assessed if the goal is cap-rock integrity analysis for SAGD applications.

It is important to consider the scale of the coarse blocks. As shown, error increases with increasing upscaling ratios. For a given problem, the acceptable error in the response should be quantified by the practitioner and an appropriate block size selected. This is standard practice in flow simulation where past experience can be relied upon to select an appropriate coarse scale; however, in geomechanical simulation, homogenous property models dominate and there is little guidance on upscaled block size selection.

The difficulty with considering analytical upscaling methods is determining their range of applicability as they are sensitive to parameter calibration. It may be inappropriate to apply analytical techniques to new geological situations beyond their intended use. Conversely, the proposed numerical technique is appropriate for various domains that can be characterized by transverse isotropy.

References

Backus, G. 1962. Long-wave elastic anisotropy produced by horizontal layering. Journal Geophysical Research. 67: 11, 4427–11, 4440.

Budiansky, B. 1965. On the elastic moduli of some heterogeneous materials. Journal of the Mechanics and Physics of Solids 13:223–227.

Deutsch, C.V. 1989. Calculating Effective Absolute Permeability in Sandstone/Shale Sequences. SPE Formation Evaluation. 4: 3,343–3,348.

Deutsch, C. V. and A. G Journel. 1998. GSLIB: Geostatistical Software Library and User's Guide. Second edition, Oxford, New York

Durlofsky, L. J. 1991. Numerical calculation of equivalent grid block permeability tensors for heterogeneous porous media. *Water Resources Research.* 27: 5,669–5,708

Durlofsky, L.J. 2005. Upscaling and gridding of fine scale geological models for flow simulation. Presented at 8th international forum of reservoir simulation, Stresa, Italy.

Elkateb, T. M. 2003. Quantification of Soil Heterogeneity. PhD dissertation, University of Alberta, Edmonton, Canada.

Hashin, Z. 1955. The moduli of an elastic solid reinforced by rigid particles. Bulletin of the Research Council of Israel 5C:46–59.

Hill, R. 1965. A self-consistent mechanics of composite materials. Journal of the Mechanics and Physics of Solids 13:213–222.

Kasap, E. and L. W. Lake. 1990. Calculating the effective permeability tensor of a gridblock. SPE Formation Evaluation. 5:192–200.

King, M. J. and M. Mansfield. 1999. Flow simulation of geologic models. SPE Reservoir Evaluation & Engineering. 2: 351–367.

Lekhnittskii, S.G. 1981. Theory of Elasticity of an Anisotropic Body. Moscow: Mir Publishers

Mackenzie, J. 1950. The elastic constants of a solid containing spherical holes. Proceedings of the Royal Society London 63: 1,2–1,11.

Norris, R.J. and Lewis, J. M. 1991. The geological modeling of effective permeability in complex heterolithic facies. In Proceeding of the 66th Annual Technical Conference and Exhibition, SPE 22692 Dallas, Texas, USA, Vol. W, pp. 359-374.

Pickup, G.E., P.S. Ringrose, J.L. Jensen and K.S. Sorbie .1994. Permeability tensors for sedimentary structures. Mathematical Geology. 26: 2–227,2–250

Salamon, M. 1968. Elastic moduli of a stratified rock mass. Journal of Rock Mechanics and Mining Sciences 5:519–527.

Tables

Table 1. Material properties in each section of Figure 7.

	Overburden	Side Burden	Under burden	Central Section
Deformation type	Isotropic	Isotropic	Isotropic	Transversely Isotropic
Young modulus (MPa)	250	480	5000	Shale : 300
				Sand : 600
Poison Ratio	0.3			Shale : 0.3
				Sand : 0.3

Table 2. Number of grid cells.

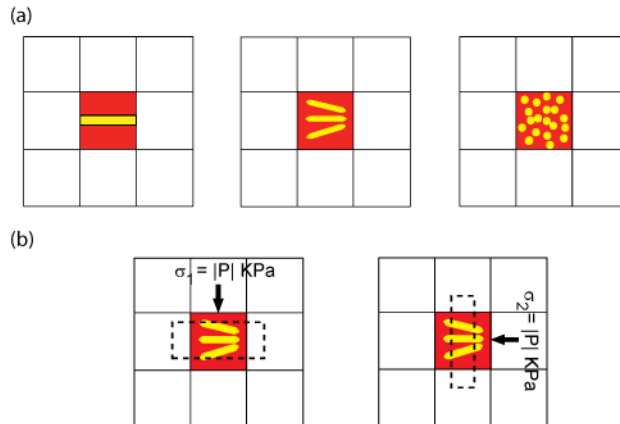|	Overburden	Side Burden	Under burden	Central Section
Horizontal	360	30	360	300
Vertical	10	40	10	40

Figures

Figure 2. (a) Three different distributions of facies with the same proportion for each facies. (b) Anisotropic deformation.
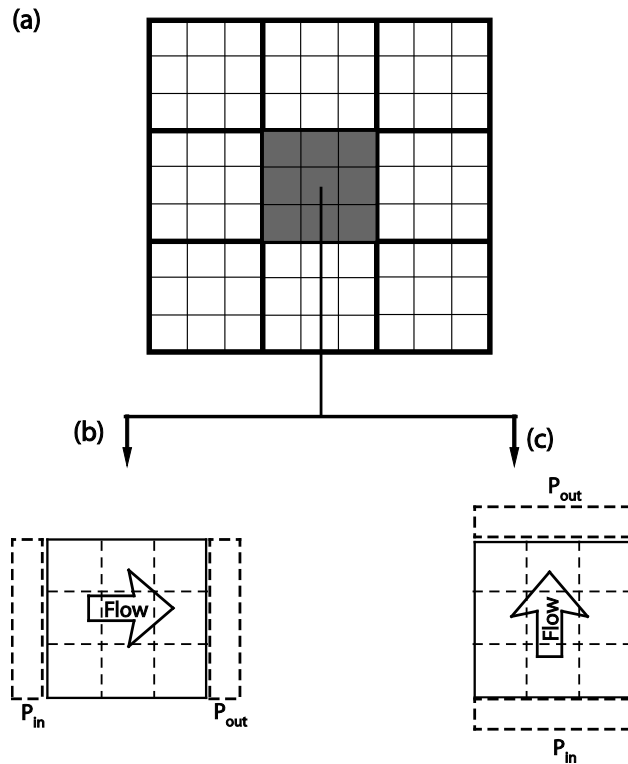

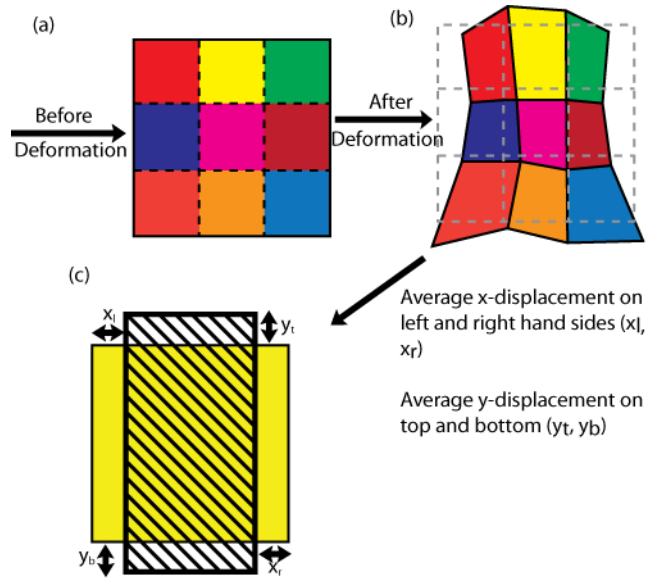
Figure 2. Schematic of pure local upscaling.
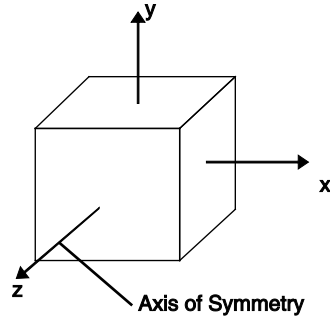
Figure 3. Conceptual framework for numerical upscaling.

Figure 4. Plane of symmetry for transversely isotropic materials.
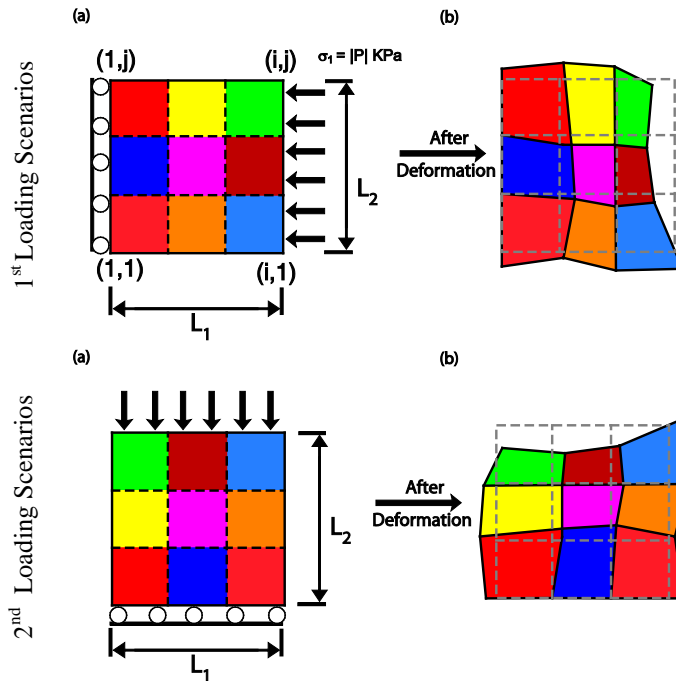
Figure 5. Initial boundary conditions for loading scenarios.
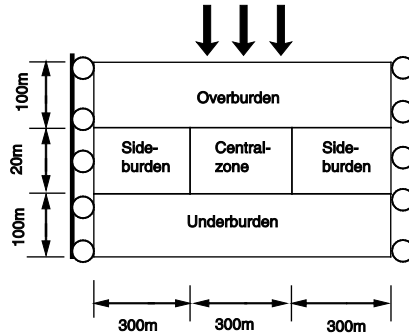
Figure 6. Geometry of the area of interest used.
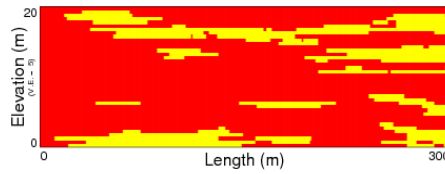
Figure 7. SIS facies realization considered with 20% shale. Red (dark) is sand; yellow (light) is shale. Variogram parameters: one spherical structure with a vertical range of 4m, horizontal range of 120m and no nugget effect.
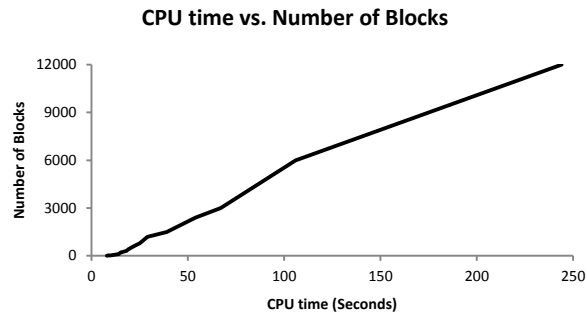
CPU time vs. Number of Blocks

Figure 8. CPU time for geomechanical simulation of the model in Figure 7.
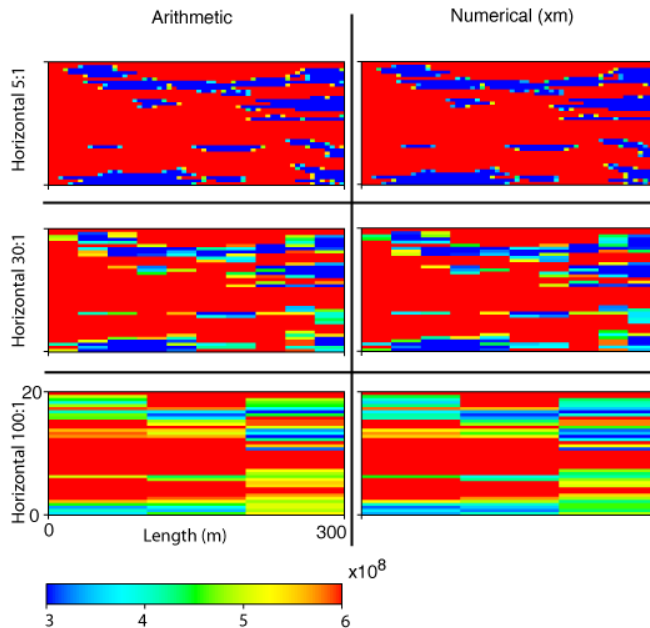
Figure 9. Young modulus for different horizontal upscaling ratios, vertical upscaling ratio is constant at 1:1.
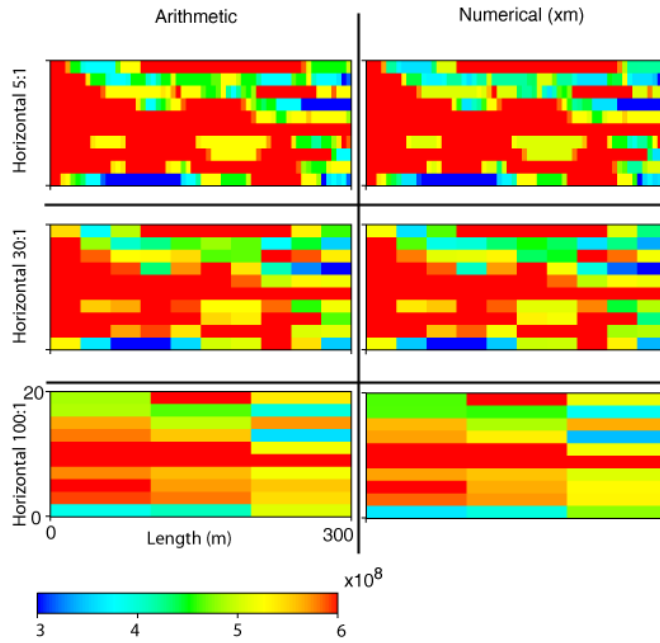
Figure 10. Young modulus for different horizontal upscaling ratios, vertical upscaling ratio is constant at 4:1.
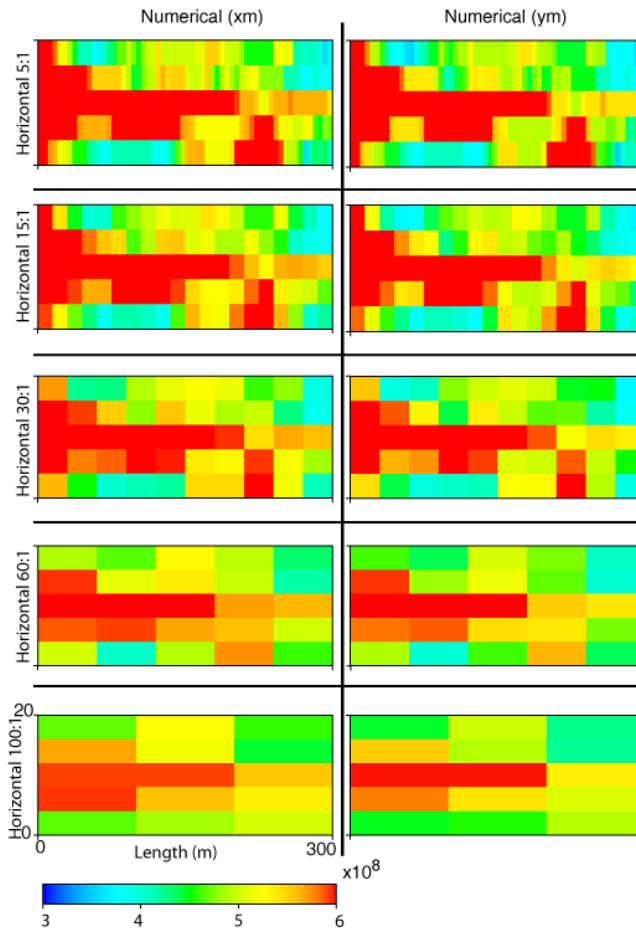

Figure 11. Young modulus for different horizontal upscaling ratios, vertical upscaling ratio is constant at 8:1.

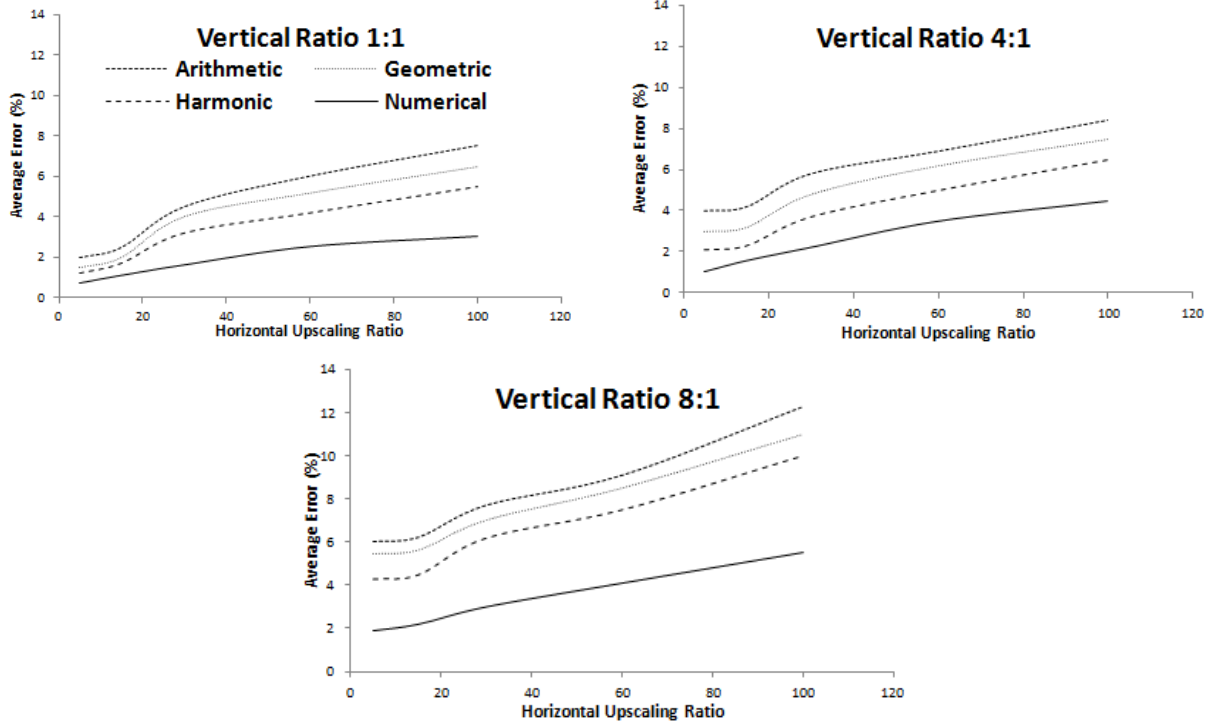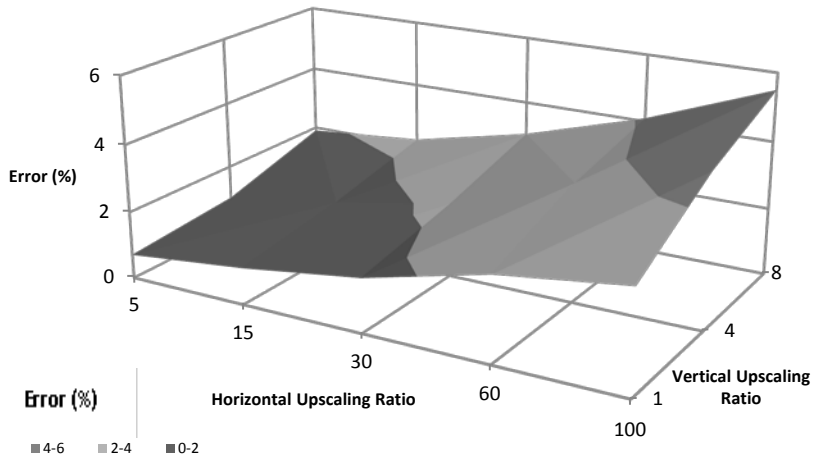**Figure 12. Average error for various horizontal and vertical upscaling ratios**

Figure 13. Error surface map for numerical upscaling.